# SURFACE TEMPERATURE EFFECTS IN LOW-DENSITY FLOW OVER FLAT-NOSE BODIES AT HYPERSONIC SPEED. PART II: AERODYNAMIC SURFACE QUANTITIES

**Wilson F. N. Santos**
National Institute for Space Research
Combustion and Propulsion Laboratory
12630-000 Cachoeira Paulista, SP, Brazil
wilson@lcp.inpe.br

**Abstract.** *The successful design of high-lift, low-drag hypersonic configurations depends on the ability to incorporate sharp/blunt leading edges that combine good aerodynamic properties with acceptable heating rates. In this study, the flow around a family of flat-nose leading edges at zero incidence is investigated by using the Direct Simulation Monte Carlo (DSMC) method. Effects of variation on the body surface temperature and on the leading edge thickness are investigated in terms of the aerodynamic surface quantities. The aerothermodynamic performance of the flat-nose leading edges is assessed by using the pressure, skin friction, heat transfer and total drag coefficients. The calculation results depict a weak effect of the leading edge thickness and of the wall temperature on total drag, while predict a strong dependence of stagnation point heating on the leading edge thickness over the range examined. The data generated in the present study is part of an investigation in order to determine the benefits and disadvantages of using these new blunt shapes over circular cylinder shapes.*

*Keywords. DSMC, aerodynamic heating, hypersonic flow, rarefied flow, blunt leading edge.*

## 1. Introduction

At hypersonic flight speeds, the vehicle leading edge must be blunt to some extent in order to reduce the heat transfer rate to acceptable levels and to allow for internal heat conduction. The use of blunt-nose shapes tends to alleviate the aerodynamic heating problem since the heat flux for blunt bodies is far lower than that for sharply pointed bodies. In addition, the reduction in heating rate for a blunt body is accompanied by an increase in heat capacity, due to the increased volume. Due mainly to manufacturing problems and the extremely high temperatures attained in hypersonic flight, hypersonic vehicles will have blunt nose, although probably slendering out at a short distance from the nose. Therefore, designing a hypersonic vehicle leading edge involves a tradeoff between making the leading edge sharp enough to obtain acceptable aerodynamic and propulsion efficiency and blunt enough to reduce the aerodynamic heating in the stagnation point.

A method of designing low heat transfer bodies is devised on the premise that the rate of heat transfer to the nose will be low if the local velocity is low, while the rate of heat transfer to the afterbody will be low if the local density is low (Reller, 1957). A typical body that results from this design method consists of a flat nose followed by a highly curved, but for the most part slightly inclined, afterbody surface. In this connection, Santos (2003) has investigated the effect of the leading edge thickness on the flowfield structure over these flat-nose leading edges. The thickness effect was examined for a range of Knudsen number, based on the thickness of the flat nose, covering from the transitional flow regime to the free molecular flow regime. The emphasis of the work was to compare the heat transfer and drag of these new flat-nose leading edges with those obtained for circular cylinder shape, typically assumed as the appropriate blunting geometry for heat transfer considerations. It was found that flat-nose leading edges provided much smaller drag than round leading edges. Nevertheless, round leading edge still gave smaller stagnation point heating than the flat-nose leading edges for the conditions investigated. Moreover, flat-nose bodies have more volume than the round leading edges. In this respect, the overall heat transfer to these leading edges may be tolerate if there is active cooling, since additional coolant may be placed in the leading edge.

In order to provide information on how well these shapes stand up as possible candidates for blunting geometries of hypersonic leading edges, this paper extends the analysis presented by Santos (2003) by performing a parametric study on these shapes with a great deal of emphasis placed on the wall temperature effects. In this scenario, the primary aim is to assess the sensitivity of the pressure, skin friction, heat transfer and drag coefficients to variations on the body surface temperature.

The focus of the present study is the low-density region in the upper atmosphere, where numerical gaskinetic procedures are available to simulate hypersonic flows. High-speed flows under low-density conditions deviate from a perfect gas behavior because of the excitation of rotation, vibration and dissociation. At high altitudes, and therefore, low density, the molecular collision rate is low and the energy exchange occurs under nonequilibrium conditions. In such a circumstance, the degree of molecular nonequilibrium is such that the Navier-Stokes equations are inappropriate. Therefore, the DSMC method will be employed to calculate the hypersonic two-dimensional flow on the leading edges.

## 2. Body Shape Definition

In dimensionless form, the contour that defines the shape of the afterbody surface is given by,

$$\overline{x} = \int_{\overline{y}=1}^{\overline{y}=\overline{y}_{max}} \sqrt{\overline{y}^k - 1} d\overline{y} \tag{1}$$

where $\overline{x} = x/y_{nose}$ and $\overline{y} = y/y_{nose}$ .

The blunt shapes are modeled by assuming a sharp leading edge of half angle $\theta$ with a circular cylinder of radius $R$ inscribed tangent to the wedge. The blunt shapes, inscribed between the wedge and the cylinder, are also tangent to them at the same common point where they have the same slope angle. The circular cylinder diameter provides a reference for the amount of blunting desired on the leading edges. It was assumed a leading edge half angle of 10 degrees, a circular cylinder diameter of $10^{-2}$m and flat-nose thicknesses $t/\lambda_\infty$ of 0.01, 0.1 and 1, where $t = 2y_{nose}$ and $\lambda_\infty$ is the freestream mean free path. Figure (1a) illustrates this construction for the set of shapes investigated. From geometric considerations, the exponent $k$ in Eq. (1) is obtained by matching slope on the wedge, circular cylinder and on the body shapes at the tangency point. For dimensionless thicknesses of 0.01, 0.1 and 1, the exponent $k$ corresponds to 0.501, 0.746 and 1.465, respectively. The common body height $H$ and the body length $L$ are obtained in a straightforward manner. It was assumed that the leading edges are infinitely long but only the length $L$ is considered, since the wake region behind the leading edges is not of interest in this investigation.
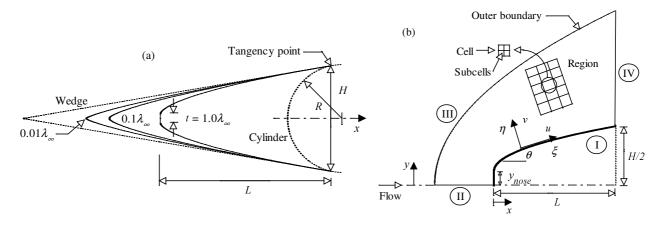


Figure 1: Drawing illustrating (a) the leading edge shapes and (b) the computational domain.

## 3. Computational Method and Procedure

It is well known that conventional fluid dynamics is applicable to flows with Knudsen numbers $Kn = \lambda/l < 0.1$, where $\lambda$ is the molecular mean free path and $l$ is the characteristic length of the problem. Nevertheless, mathematical modeling of flows with $Kn \geq 0.1$ is supposed to be based on the solution of the Boltzmann equation (Cercignani, 1988) or on the Direct Simulation Monte Carlo (DSMC) method (Bird, 1994).

The DSMC method simulates real gas flows with various physical processes by means of a huge number of modeling particles, each particle represents a fixed number of real gas molecules. In this fashion, the number of molecular trajectories and molecular collisions that must be calculated is substantially reduced, while the molecular size, the physical velocities and internal energies are preserved in the simulation. In the DSMC model, the particle evolution is divided into two independent phases during the simulation; the movement phase and the collision phase. In the movement phase, all particles are moved over distances appropriate to a short time interval, time step, and some of them interact with the domain boundaries in this time interval. Particles that strike the solid wall would reflect according to the appropriate gas-surface interaction model, specular, diffusive or a combination of these. In the collision phase, intermolecular collisions are performed according to the theory of probability without time being consumed. In this context, the intermolecular collisions are uncoupled to the translational molecular motion over the time step used to advance the simulation. Time is advanced in discrete steps such that each step is small in comparison with the mean collision time (Garcia and Wagner, 2000, and Hadjiconstantinou, 2000). The simulation is always calculated as unsteady flow. However, a steady flow solution is obtained as the large time state of the simulation.

The molecular collisions are modeled using the variable hard sphere (VHS) molecular model (Bird, 1981) and the no time counter (NTC) collision sampling technique (Bird, 1989). The VHS model employs the simple hard sphere angular scattering law so that all directions are equally possible for post-collision velocity in the center-of-mass frame

of reference. However, the collision cross section depends on the relative speed of colliding molecules. The energy exchange between kinetic and internal modes is controlled by the Borgnakke-Larsen statistical model (Borgnakke and Larsen, 1975). The essential feature of this model is that a part of collisions is treated as completely inelastic, and the remainder of the molecular collisions is regarded as elastic. Simulations are performed using a nonreacting gas model consisting of two chemical species, $N_2$ and $O_2$. Energy exchanges between the translational and internal modes are considered. For a given collision, the probabilities are designated by the inverse of the relaxation numbers, which correspond to the number of collisions necessary, on average, for a molecule to relax. In this simulation, the relaxation number is 5 for rotation and 50 for vibration.

In order to implement the particle-particle collisions, the flowfield is divided into an arbitrary number of regions, which are subdivided into computational cells. The cells are further subdivided into four subcells, two subcells/cell in each direction. The cell provides a convenient reference sampling of the macroscopic gas properties, whereas the collision partners are selected from the same subcell for the establishment of the collision rate. As a result, the flow resolution is much higher than the cell resolution. The dimensions of the cells must be such that the change in flow properties across each cell is small. The linear dimensions of the cells should be small in comparison with the scale length of the macroscopic flow gradients normal to the streamwise directions, which means that the cell dimensions should be of the order of the local mean free path or even smaller (Alexander et al., 1998 and Alexander et al., 2000).

The computational domain used for the calculation is made large enough so that body disturbances do not reach the upstream and side boundaries, where freestream conditions are specified. A schematic view of the computational domain is depicted in Fig. (1b). Side I is defined by the body surface. Diffuse reflection with complete thermal accommodation is the condition applied to this side. In a diffuse reflection, the molecules are reflected equally in all directions, and the final velocity of the molecules is randomly assigned according to a half-range Maxwellian distribution determined by the wall temperature. Advantage of the flow symmetry is taken into account, and molecular simulation is applied to one-half of a full configuration. Thus, side II is a plane of symmetry. In such a boundary, all flow gradients normal to the plane are zero. At the molecular level, this plane is equivalent to a specular reflecting boundary. Side III is the freestream side through which simulated molecules enter and exit. Finally, the flow at the downstream outflow boundary, side IV, is predominantly supersonic and vacuum condition is specified (Guo and Liaw, 2001). At this boundary, simulated molecules can only exit.

Numerical accuracy in DSMC method depends on the grid resolution chosen as well as the number of particles per computational cell. Both effects were investigated to determine the number of cells and the number of particles required to achieve grid independence solutions. Grid independence was tested by running the calculations with half and double the number of cells in $\xi$ and $\eta$ directions (see Fig. (1b)) compared to a standard grid. Solutions (not shown) were near identical for all grids used and were considered fully grid independent.

The freestream and flow conditions used in the present calculations are those given by Santos (2003) and summarized in Tab. (1). The gas properties considered in the simulation are those given by Bird (1994) and shown in Tab. (2). The freestream velocity $V_\infty$, assumed to be constant at 3.56 km/s, corresponds to a freestream Mach number $M_\infty$ of 12. In order to simulate the body surface temperature effects, the wall temperature $T_w$ is assumed constant at 440, 660, 880 and 1100 K, which correspond to 2, 3, 4 and 5 times the freestream temperature.

Table 1: Freestream Conditions

| Temperature $T_\infty$ (K) | Pressure $p_\infty$ (N/m$^2$) | Density $\rho_\infty$ (kg/m$^3$) | Number density $n_\infty$ (m$^{-3}$) | Viscosity $\mu_\infty$ (Ns/m$^2$) | Mean free path $\lambda_\infty$ (m) | Velocity $V_\infty$ (m/s) |
|---|---|---|---|---|---|---|
| 220.0 | 5.582 | 8.753 x 10$^{-5}$ | 1.8209 x 10$^{21}$ | 1.455 x 10$^{-5}$ | 9.03 x 10$^{-4}$ | 3560 |

Table 2: Gas Properties

| | Mole fraction $X$ | Molecular mass $m$ (kg) | Molecular diameter $d$ (m) | Viscosity Index $\omega$ |
|---|---|---|---|---|
| $O_2$ | 0.237 | 5.312 x 10$^{-26}$ | 4.01 x 10$^{-10}$ | 0.77 |
| $N_2$ | 0.763 | 4.65 x 10$^{-26}$ | 4.11 x 10$^{-10}$ | 0.74 |

The overall Knudsen number $Kn_t$, defined as the ratio of the freestream mean free path $\lambda_\infty$ to the leading edge thickness $t$, corresponds to 100, 10 and 1 for leading edge thicknesses $t/\lambda_\infty$ of 0.01, 0.1 and 1, respectively. The Reynolds number $Re_t$ covers the range from 0.193 to 19.3, based on conditions in the undisturbed stream with leading edge thickness $t$ as the characteristic length.

## 4. Computational Results and Discussions

This section focuses on the effects that take place in the aerodynamic surface quantities due to the variations on the leading edge thickness and on the wall temperature. Aerodynamic surface quantities of particular interest in the

transition flow regime are number flux, heat transfer, pressure, skin friction and drag. In this scenario, this section discusses and compares differences of these quantities expressed in coefficient form.

### 4.1. Number Flux

As the body surface temperature is increased from 440 to 1100 K, the molecules impinging on the body surface are reflected with greater energies. In this connection, the relative translational velocities of reflected molecules close to the body surface will be increased, thus reducing the net buildup of particle density near the body surface. As a result, changes in the number of molecules colliding with the body surface as well as changes in the incident and reflected momentum and energy of these molecules are expected.

The number flux $N$ is calculated by sampling the molecules impinging on the surface by unit time and unit area. The sensitivity of the dimensionless number flux to variations on the leading edge thickness and on the body surface temperature is illustrated in Figs. (2a) and (2b) for leading edge thicknesses $t/\lambda_\infty$ of 0.01 and 1, that correspond to $Kn_t$ of 100 and 1, respectively. In this set of figures, the dimensionless number flux stands for the number flux $N$ normalized by $n_\infty V_\infty$, where $n_\infty$ is the freestream number density and $V_\infty$ is the freestream velocity. Also, $S$ is the arc length $s$ along the body surface, measured from the stagnation point, normalized by the freestream mean free path $\lambda_\infty$.

According to these plots, the dimensionless number flux to the surface relies not only on the leading edge thickness but also on the body surface temperature. For a sharp leading edge, $Kn_t$ of 100 ($t/\lambda_\infty = 0.01$), the dimensionless number flux is low and constant along the frontal surface and decreases gradually along the afterbody surface. A similar behavior is seen (not shown) for the slightly blunt leading edge case, $Kn_t$ of 10 ($t/\lambda_\infty = 0.1$). On the other hand, for the bluntest leading edge case investigated, $Kn_t$ of 1 ($t/\lambda_\infty = 1$), the dimensionless number flux is large on the frontal surface. It presents a constant value in the first half of the flat face and decreases in the vicinity of the shoulder. After that, it decreases significantly along the afterbody surface. One possible reason for this increase in the dimensionless number flux with increasing the leading edge thickness may be related to the collisions of two groups of molecules; the molecules reflecting from the body and the molecules oncoming from the freestream. The molecules that are reflected from the body surface, which have a lower kinetic energy interact with the oncoming freestream molecules, which have a higher kinetic energy. Thus, the surface-reflected molecules recollide with the body surface, which produce an increase in the dimensionless number flux in this region. As expected, this behavior is less pronounced with increasing the body surface temperature, since the molecules are reflected from the surface with greater energies. Consequently, the net buildup of particle density near the body surface is reduced.

For comparison purpose, the dimensionless number flux by considering free molecular flow is also displayed in Figs. (2a) and (2b). It is seen from Fig. (2a) that, for the $Kn_t = 100$ case, the dimensionless number flux along the frontal surface approaches the limit value, $N/n_\infty V_\infty = 1$, obtained by the free molecular flow equations (Bird, 1994).
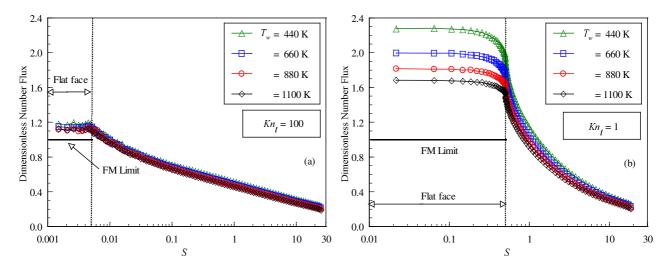


Figure 2: Dimensionless number flux ($N/n_\infty V_\infty$) along the body surface as a function of the wall temperature for leading edge thicknesses that correspond to Knudsen number $Kn_t$ of (a) 100 and (b) 1.

### 4.2. Heat Transfer Coefficient

The heat transfer coefficient $C_h$ is defined as being,

$$C_h = \frac{q_w}{\frac{1}{2}\rho_\infty V_\infty^3} \tag{2}$$

where $q_w$ is the net heat flux to the body surface and $\rho_\infty$ is the freestream density.

The heat flux $q_w$ to the body surface is calculated by the net energy flux of the molecules impinging on the surface. A flux is regarded as positive if it is directed toward the surface. The net heat flux $q_w$ is related to the sum of the translational, rotational and vibrational energies of both incident and reflected molecules as defined by,

$$q_w = q_i + q_r = \sum_{j=1}^{N} \left\{ \left[ \frac{1}{2} m_j v_j^2 + e_{Rj} + e_{Vj} \right]_i + \left[ \frac{1}{2} m_j v_j^2 + e_{Rj} + e_{Vj} \right]_r \right\} \tag{3}$$

where $N$ is the number of molecules colliding with the surface by unit time and unit area, $m$ is the mass of the molecules, $v$ is the velocity of the molecules, $e_R$ and $e_V$ stand for the rotational and vibrational energies, respectively. Subscripts $i$ and $r$ refer to incident and reflected molecules.

Distribution of heat transfer coefficient along the body surface is plotted in Fig. (3) parameterized by the wall temperature. It is noticed from Fig. (3) that the heat transfer coefficient is sensitive to the leading edge thickness as well as to the body surface temperature. The heat transfer coefficient remains essentially constant over the first half of the front surface, but then increases in the vicinity of the flat-face/afterbody junction for the bluntest case investigated, $Kn_t = 1$ ($t/\lambda_\infty = 1$). Subsequently, the heat transfer coefficient decreases sharply and continues to decline along the body surface. As would be expected, the blunter the leading edge is the lower the heat transfer coefficient at the stagnation point. Moreover, the higher the wall temperature the lower the heat transfer coefficient along the frontal surface and in the vicinity of the flat-face/afterbody junction. For the purpose of reference, the heat transfer coefficient at the stagnation point for shapes $t/\lambda_\infty = 0.01$, 0.1 and 1 at $T_w = 440$ K corresponds, respectively, to 1.14, 1.12 and 1.12 times the heat transfer coefficient for the same shapes at $T_w = 1100$ K.
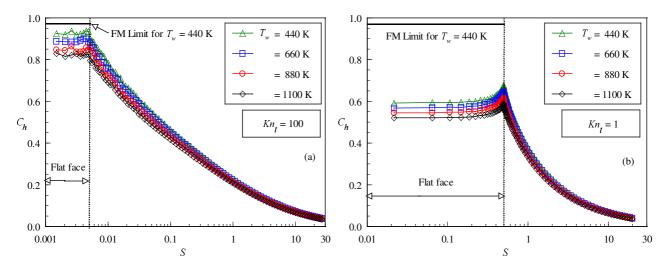


Figure 3: Heat transfer coefficient $C_h$ along the body surface as a function of the wall temperature for leading edge thicknesses that correspond to Knudsen number $Kn_t$ of (a) 100 and (b) 1.

Of particular interest is the behavior of the heat transfer coefficient in the vicinity of the flat-face/afterbody junction. As the number of molecules impinging on the body surface decreases (see Fig. (2)) in the vicinity of the leading edge shoulder, then the velocity of the molecules increases in this region in order to increase the heat transfer coefficient in this region. As a matter of fact, a molecular velocity rise in this region is expected due to the flow expansion along the shoulder of the leading edge.

The heat flux to the body surface was defined in terms of the incident and reflected flow properties (see Eq.(3)) and based upon the gas-surface interaction model of fully accommodated, complete diffuse re-emission. The diffuse model assumes that the molecules are reflected equally in all directions, quite independently of their incident speed and direction. Due to the diffuse reflection model, the reflected velocity of the molecules impinging on the body surface is obtained from a Maxwellian distribution that takes into account for the temperature of the body surface. In this fashion, according to Eq.(3), not only the number of molecules impinging on the surface but also the wall temperature plays a important role on the reflected contribution to the net heat flux to the body surface. In order to elucidate this behavior, Fig. (4) depicts the incident and reflected components of the heat transfer coefficient for the $Kn_t = 1$ ($t/\lambda_\infty = 1$) case.

According to Fig. (4), it is observed that the incident heat flux contributes to increase the heat transfer coefficient along the frontal surface of the leading edge. With the wall temperature rise, the buildup of particle density near the body surface is reduced (Santos, 2004), allowing the molecules oncoming from the freestream to transfer more energy to the body surface. Nevertheless, with increasing the wall temperature, the reflected heat flux also increases, and results in lower net heat flux, according to Eq. (3).
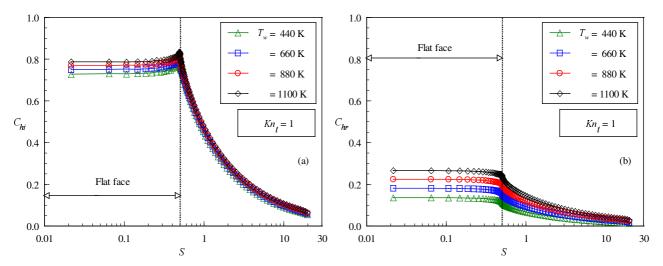
Figure 4: (a) Incident heat transfer coefficient $C_{hi}$ and (b) reflected heat transfer coefficient $C_{hr}$ along the body surface as a function of the wall temperature for leading edge thickness that correspond to Knudsen number $Kn_t$ of 1.

## 4.3. Pressure Coefficient

The pressure coefficient $C_p$ is defined as being,

$$C_p = \frac{p_w - p_\infty}{\frac{1}{2}\rho_\infty V_\infty^2}$$ (4)

where $p_w$ is the pressure acting on the body surface and $p_\infty$ is the freestream pressure.

The pressure $p_w$ on the body surface is calculated by the sum of the normal momentum fluxes of both incident and reflected molecules at each time step as follows,

$$p_w = p_i + p_r = \sum_{j=1}^{N} \left\{ \left[ m_j v_{\eta j}^2 \right]_i + \left[ m_j v_{\eta j}^2 \right]_r \right\}$$ (5)

where $v_\eta$ is the normal velocity component of the molecules (see Fig. (1b)).

The effect on pressure coefficient due to variations on the leading edge thickness and on the wall temperature is demonstrated in Fig. (5). Figure (5a) displays the pressure coefficient along the body surface for the $Kn_t = 100$ ($t/\lambda_\infty = 0.01$) case, and Fig. (5b) for the $Kn_t = 1$ ($t/\lambda_\infty = 1$) case, the bluntest case investigated. The results for pressure coefficient as well as for the other surface quantities corresponding to the $Kn_t = 10$ ($t/\lambda_\infty = 0.1$) case have been leaved out because they are intermediate to the other cases shown. Plotted along with the computational solutions for pressure coefficient is the pressure coefficient limit predicted by the free molecular flow. It is found from the free molecular flow equations values for $C_p$ along the frontal surface of 2.25, 2.31, 2.35 and 2.39 for wall temperature of 440, 660, 880 and 1100 K, respectively. As expected, the pressure coefficient along the frontal surface for the $Kn_t = 100$ case approaches the free molecular limit, as shown in Fig. (5a).

Referring to Fig. (5), it is found that the wall temperature rise investigated has no expressive effect on the pressure coefficient for the bluntest leading edge ($Kn_t = 1$), whereas it increases slightly the pressure coefficient on the frontal surface for the sharpest case ($Kn_t = 100$) investigated. At this point, it is important to recognize from the number flux distribution in Fig. (2) that significant changes in the number flux occur due to variations not only on the leading edge thickness but also on the wall temperature.

In what follows, for convenience, the pressure coefficient is further evaluated in Fig. (6), that shows separately the contributions of incident and reflected components of the wall pressure along the body surface for the $Kn_t = 1$ ($t/\lambda_\infty = 1$) case. It is apparent from these plots that the energetic scattered molecules play a more significant role, since the incident component of the pressure coefficient decreases and the reflected one increases with increasing the wall temperature. Hence, the insensitivity of the pressure coefficient to wall temperature variations in the range investigated, shown in Fig. (5), is primarily attributed to a counterbalance between the number flux reduction and the normal momentum rise related to the reflected molecules.
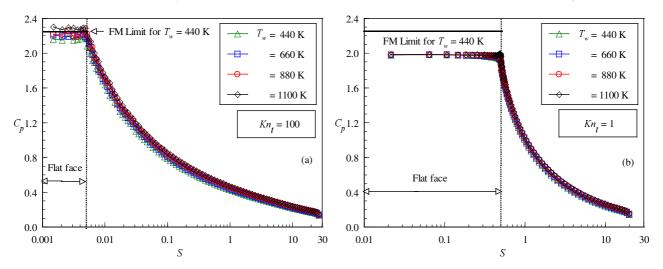
Figure 5: Pressure coefficient $C_p$ along the body surface as a function of the wall temperature for leading edge thicknesses that correspond to Knudsen number $Kn_t$ of (a) 100 and (b) 1.
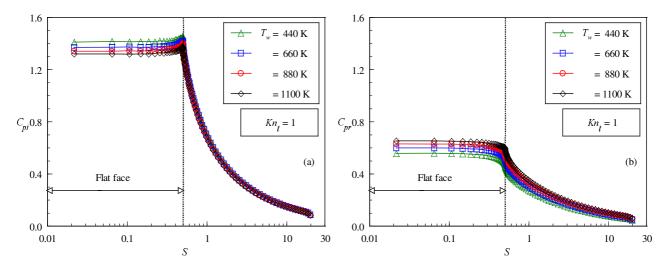
Figure 6: (a) Incident pressure coefficient $C_{pi}$ and (b) reflected pressure coefficient $C_{pr}$ along the body surface as a function of the wall temperature for leading edge thickness that correspond to Knudsen number $Kn_t$ of 1.

## 4.4. Skin Friction Coefficient

The skin friction coefficient $C_f$ is defined as being,

$$C_f = \frac{\tau_w}{\frac{1}{2}\rho_\infty V_\infty^2} \qquad (6)$$

where $\tau_w$ is the shear stress acting on the body surface.

The shear stress $\tau_w$ on the body surface is calculated by averaging the tangential momentum transfer of the molecules impinging on the surface. For the diffuse reflection model imposed for the gas-surface interaction, reflected molecules have a tangential moment equal to zero, since the molecules essentially lose, on average, their tangential velocity component. In this context, the tangential momentum flux of the incident molecules is defined as follows,

$$\tau_w = \sum_{j=1}^{N} m_j v_{\xi j}^2 \qquad (7)$$

where $v_\xi$ is the tangential velocity component of the molecules.

The variation of skin friction coefficient $C_f$ with wall temperature is depicted in Figs. (7a) and (7b) for $Kn_t$ of 100 and 1, respectively. It is noted that the skin friction coefficient is zero at the stagnation point and slightly increases

along the front surface up to the flat-face/afterbody junction of the leading edge. After that, it increases dramatically to a maximum value that depends on the leading edge thickness, and decreases downstream along the body surface. Smaller thickness $t$ (larger $Kn_t$) leads to higher peak value for the skin friction coefficient. Also, smaller thickness $t$ displaces the peak value to near the flat-face/afterbody junction.

Of particular interest in Fig. (7) is the effect of wall temperature rise on the skin friction coefficient. It is found that the skin fiction is not sensitive to wall temperature variation, provided that the gas-surface interaction is diffuse, as was assumed in this simulation. The overall shear stress $\tau_w$ is zero for fully specular reflection and is entirely due to the incident molecules for fully diffuse reflection.

The wall temperature effect on the skin friction coefficient can also be seen in a different way by comparing the DSMC computational results along the afterbody surface with that calculated by assuming free molecular flow. Figures (8) illustrates this comparison for the skin friction coefficient along the afterbody surface as a function of the slope angle $\theta$. Figure (8a) displays the skin friction coefficient along for the $Kn_t = 100$ ($t/\lambda_\infty = 0.01$) case, and Fig. (8b) for the $Kn_t = 1$ ($t/\lambda_\infty = 1$) case, the bluntest case investigated. In addition, in these figures, 90 degrees correspond to the station at the flat-face/afterbody junction, and 10 degrees correspond to the tangent point common to all of the shapes (see Fig. (1a)). It is noticed from Fig. (8) that the pick values for $C_f$ in the afterbody surface occur at a station that corresponds to a body slope angle around 45 degrees, similar to the value predicted by the free molecular flow equations.
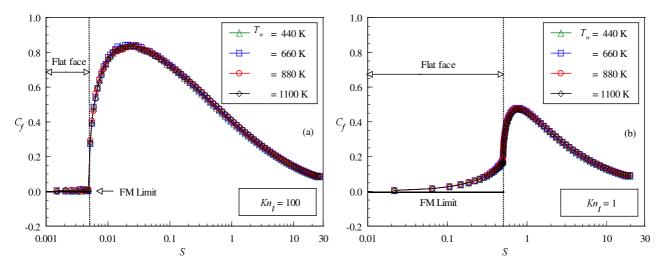


Figure 7: Skin friction coefficient $C_f$ along the body surface as a function of the wall temperature for leading edge thicknesses that correspond to Knudsen number $Kn_t$ of (a) 100 and (b) 1.
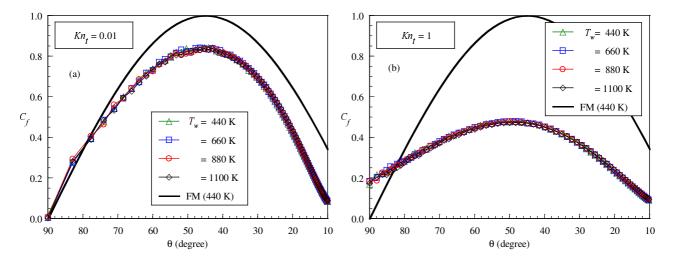


Figure 8: Skin friction coefficient $C_f$ along the afterbody surface as a function of the body slope angle for leading edge thicknesses that correspond to Knudsen number $Kn_t$ of (a) 100 and (b) 1.

## 4.5. Drag Coefficient

The total drag coefficient $C_d$ is defined as being,

$$C_d = \frac{F}{\frac{1}{2}\rho_\infty V_\infty^2 H} \tag{8}$$

where $F$ is the resultant force acting on the body surface and $H$ is the height at the matching point common to the leading edges (see Fig. (1a)).

The drag force is obtained by the integration of the pressure $p_w$ and shear stress $\tau_w$ distributions from the nose of the leading edge to the station $L$ (see Fig. (1a)), which corresponds to the tangent point common to all of the body shapes. It is important to mention that the values for the total drag presented in this section were obtained by assuming the shapes acting as leading edges. Consequently, no base pressure effects were taken into account on the calculations.

Changes in the total drag coefficient $C_d$ due to variations on the leading edge thickness and on the wall temperature are displayed in Fig. (9) for Knudsen number $Kn_t$ of 100, 10 and 1. In this set of figures, the contributions of the pressure $C_{pd}$ and skin friction drag $C_{fd}$ to the total drag coefficient are also illustrated. For comparison purpose, the total drag coefficient for the case investigated are tabulated in Table (3).

It is apparent from these set of diagrams that as the leading edge becomes blunter, i.e., the nose becomes flatter, the contribution of the pressure drag to the total drag increases and the contribution of the skin friction drag decreases, and the net effect results in a slightly increase in the total drag. It is also seen that the total drag increases slightly with increasing the wall temperature.
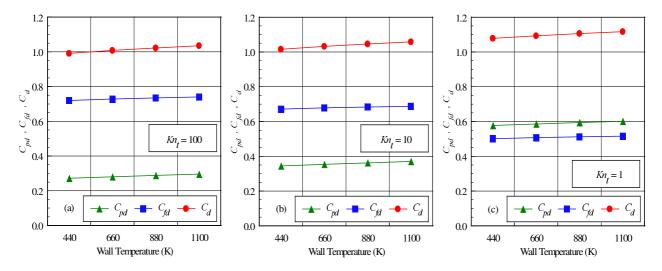


Figure 9: Pressure drag $C_{pd}$, skin friction drag $C_{fd}$ and total drag coefficient $C_d$ as a function of the wall temperature for leading edge thicknesses that correspond to Knudsen number $Kn_t$ of (a) 100 and (b) 10 and (c) 1.

Table 3: Total drag coefficient for the flat-nose leading edges.

| $T_w$ | $Kn_t = 100$ | $Kn_t = 10$ | $Kn_t = 1$ |
|---|---|---|---|
| 440 K | 0.991 | 1.016 | 1.078 |
| 660 K | 1.008 | 1.032 | 1.093 |
| 880 K | 1.022 | 1.046 | 1.105 |
| 1100 K | 1.035 | 1.058 | 1.117 |

## 5. Concluding Remarks

The Direct Simulation Monte Carlo method is used to numerically simulate the rarefied hypersonic flow on blunt leading edges. The calculations provided information concerning the nature of the aerodynamic surface quantities for a family of contours composed by a flat nose followed by a highly curved aferbody surface. Effects of body surface temperature on the number flux, heat transfer coefficient, pressure coefficient, skin friction coefficient and total drag coefficient for a wide range of parameters are investigated. The wall temperature was varied from 440 K to 1100 K, which corresponds from 2 to 5 times the freestream temperature. In addition, the leading edge thicknesses investigated correspond to thickness Knudsen number of 1, 10 and 100. Cases considered in this study cover the hypersonic flow from the transition regime to the free molecular one.

Performance results for leading edge thickness corresponding to thickness Knudsen number of 100 indicated that the aerodynamic surface quantities approach those values predicted by the free molecular flow equations on the frontal surface for the flow conditions considered. Calculations showed that the heat transfer coefficient decreases not only with increasing the leading edge thickness but also with the wall temperature rise. It was also found that the total drag

slightly increases by increasing the leading edge thickness as well as the wall temperature.

## 6. References

Alexander, F. J., Garcia, A. L., and, Alder, B. J., 1998, "Cell Size Dependence of Transport Coefficient in Stochastic Particle Algorithms", Physics of Fluids, Vol. 10, No. 6, pp. 1540-1542.

Alexander, F. J., Garcia, A. L., and, Alder, B. J., 2000, "Erratum: Cell Size Dependence of Transport Coefficient is Stochastic Particle Algorithms", Physics of Fluids, Vol. 12, No. 3, pp. 731-731.

Bird, G. A., 1981, "Monte Carlo Simulation in an Engineering Context", Progress in Astronautics and Aeronautics: Rarefied gas Dynamics, Ed. Sam S. Fisher, Vol. 74, part I, AIAA New York, pp. 239-255.

Bird, G. A., 1989, "Perception of Numerical Method in Rarefied Gasdynamics", Rarefied gas Dynamics: Theoretical and Computational Techniques, Eds. E. P. Muntz, and D. P. Weaver and D. H. Capbell, Vol. 118, Progress in Astronautics and Aeronautics, AIAA, New York, pp. 374-395.

Bird, G. A., 1994, "Molecular Gas Dynamics and the Direct Simulation of Gas Flows", Oxford University Press, Oxford, England, UK.

Borgnakke, C. and Larsen, P. S., 1975, "Statistical Collision Model for Monte Carlo Simulation of Polyatomic Gas Mixture", Journal of computational Physics, Vol. 18, No. 4, pp. 405-420.

Cercignani, C., 1988, "The Boltzmann Equation and Its Applications", Springer-Verlag, New York, NY.

Garcia, A. L., and, Wagner, W., 2000, "Time Step Truncation Error in Direct Simulation Monte Carlo", Physics of Fluids, Vol. 12, No. 10, 2000, pp. 2621-2633.

Guo, K. and Liaw, G.-S., 2001, "A Review: Boundary Conditions for the DSMC Method", Proceedings of the 35th AIAA Thermophysics Conference, AIAA Paper 2001-2953, Anaheim, CA, 11-14 June.

Hadjiconstantinou, N. G., 2000, "Analysis of Discretization in the Direct Simulation Monte Carlo", Physics of Fluids, Vol. 12, No. 10, pp. 2634-2638.

Haas, B. L., and Fallavollita, M. A., 1994, "Flow Resolution and Domain Influence in Rarefied Hypersonic Blunt-Body Flows", Journal of Thermophysics and Heat Transfer, Vol. 8, No. 4, pp. 751-757.

Nonweiler, T. R. F., 1959, "Aerodynamic Problems of Manned Space Vehicles", Journal of the Royal Aeronautical Society, Vol. 63, Sept, pp. 521-528.

Reller Jr., J. O., 1957, "Heat Transfer to Blunt Nose Shapes with Laminar Boundary Layers at High Supersonic Speeds", NACA RM-A57FO3a.

Santos, W. F. N., 2003, "Aerodynamic Heating on Blunt Nose Shapes in Rarefied Hypersonic Flow", Proceedings of the 17th International Congress of Mechanical Engineering COBEM 2003, 10-14 Nov, São Paulo, SP, Brazil.

Santos, W. F. N., 2004, "Surface Temperature Effects in Low-Density Flow over Flat-Nose Bodies at Hypersonic Speed. Part I: Flowfield Structure", Proceedings of the 10th Brazilian Congress of Thermal Sciences and Engineering ENCIT 2004, 29 Nov – 3 Dec, Rio de Janeiro, RJ, Brazil (Submitted).